Revisiting the Electrochemical Nitrogen Reduction on Molybdenum and Iron Carbides Promising Catalysts or False Positives?

Izelaar, Boaz; Ripepi, Davide; Asperti, Simone; Dugulan, A. Iulian; Hendrikx, Ruud W.A.; Böttger, Amarante J.; Mulder, Fokko M.; Kortlever, Ruud

DOI
10.1021/acscatal.2c04491

Publication date
2023

Document Version
Final published version

Published in
ACS Catalysis

ACS Catalysis

pubs.acs.org/acscatalysis

Research Article

Revisiting the Electrochemical Nitrogen Reduction on Molybdenum and Iron Carbides: Promising Catalysts or False Positives?

Boaz Izelaar, Davide Ripepi, Simone Asperti, A. Iulian Dugulan, Ruud W.A. Hendrikx, Amarante J. Böttger, Fokko M. Mulder, and Ruud Kortlever*

Cite This: *ACS Catal.* 2023, 13, 1649−1661

Read Online

ACCESS | Metrics & More | Article Recommendations | Supporting Information

ABSTRACT: The electrochemical dinitrogen reduction reaction (NRR) has recently gained much interest as it can potentially produce ammonia from renewable intermittent electricity and replace the Haber−Bosch process. Previous literature studies report Fe- and Mo-carbides as promising electrocatalysts for the NRR with activities higher than other metals. However, recent understanding of extraneous ammonia and nitrogen oxide contaminations have challenged previously published results. Here, we critically assess the NRR performance of several Fe- and Mo-carbides reported as promising by implementing a strict experimental protocol to minimize the effect of impurities. The successful synthesis of α-Mo_2C decorated carbon nanosheets, α-Mo_2C nanoparticles, θ-Fe_3C nanoparticles, and χ-Fe_5C_2 nanoparticles was confirmed by X-ray diffraction, scanning and transmission electron microscopy, and X-ray photoelectron and Mössbauer spectroscopy. After performing NRR chronoamperometric tests with the synthesized materials, the ammonia concentrations varied between 37 and 124 ppb and are in close proximity with the estimated ammonia background level. Notwithstanding the impracticality of these extremely low ammonia yields, the observed ammonia did not originate from the electrochemical nitrogen reduction but from unavoidable extraneous ammonia and NO_x impurities. These findings are in contradiction with earlier literature studies and show that these carbide materials are not active for the NRR under the employed conditions. This further emphasizes the importance of a strict protocol in order to distinguish between a promising NRR catalyst and a false positive.

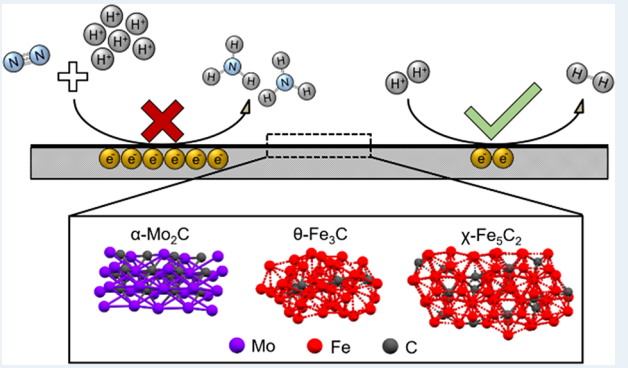

KEYWORDS: *electrocatalysis, nitrogen reduction reaction, ammonia, molybdenum, iron, carbide, impurities*

1. INTRODUCTION

The activation of diatomic nitrogen has been one of the greatest challenges in nitrogen-related chemistry.[1,2] This is inherently related to the inert nature of the nitrogen molecule due to its high bond-dissociation energy, absence of a dipole moment, and low proton and electron affinity.[3] Despite the inert nature, diazotrophic microorganisms successfully fixate nitrogen and play a key role in enriching the soil.[4] However, due to the growing world population and the high demand for food, additional nitrogen containing nutrients in the form of artificial ammonia-based fertilizers must be provided to the soil. The majority of the ammonia produced worldwide is synthesized by the Haber−Bosch process (H-B), wherein energy intensive reaction conditions (T = 300−500 °C, P = 150−300 bar) are needed to activate dinitrogen.[2] The ammonia industry consumes approximately 1% of the global energy demand and emits roughly 0.75% of the anthropogenic CO_2 emissions (assuming 1.9 t_{CO_2} $t^{-1}_{NH_3}$),[5,6] which is motivating the search for more energy efficient and sustainable alternatives.

The electrochemical nitrogen reduction reaction (NRR), wherein dinitrogen, water, and electrons from renewable sources react to form ammonia, has recently gained significant scientific interest and has been proposed as a potential replacement for the fossil fuel-based H-B.[7,8] NRR systems at high (>500 °C) and intermediate (100−500 °C) temperatures have proven to be successful in terms of faradaic efficiency (FE ≥ 75%) and NH_3 yield (≥4.5 nmol s^{-1} cm^{-2}).[9] Nevertheless, the present high temperature NRR systems tend to have a low energy efficiency compared to H-B.[10,11] Therefore, it would be beneficial to perform the NRR under ambient conditions. Significant FEs have been reported with iron electrocatalysts in ionic liquids and organic electrolytes by suppressing the

Received: September 12, 2022
Revised: December 13, 2022
Published: January 12, 2023

https://doi.org/10.1021/acscatal.2c04491
ACS Catal. 2023, 13, 1649−1661

parasitic hydrogen evolution reaction (HER).[12,13] However, the use of organic electrolytes is likely to be less economically feasible compared to aqueous electrolytes due to complex scalability, safety issues, high costs, and intense energy requirements.[8,14] Unfortunately, the kinetics under ambient conditions in aqueous electrolytes are sluggish and many attempts in examining transition metals, such as Au, Fe, Mo, Ru, Rh, and Re, as potential electrocatalysts for the NRR have resulted in low FEs (<1%) and ammonia yields (<0.1 nmol s^{-1} cm^{-2}).[15,16]

The active site of the nitrogenase enzyme, the biologic pathway for nitrogen fixation, is the FeMo-cofactor. The FeMo-cofactor contains a six iron atomic trigonal prism with a carbon-centered position. Each iron is bound to three sulfur atoms, with an additional iron and molybdenum in apical positions.[2,17] Attempts to mimic the FeMo-cofactor initiated investigation into Fe- and Mo-based heterogeneous NRR catalysts, such as carbides and sulfides. Both Mo_2C and MoS_2 show noble metal like properties, due to similar d-band configurations as Pt.[18] Therefore, they can act as cheap and robust catalytic substitutes for many applications, including water electrolysis, water gas shift reaction, and ammonia decomposition.[19] Despite the fact that these materials are good HER catalysts, several density functional theory studies have predicted favorable nitrogen binding energies.[19−21] Experimental results are somewhat distinct; nitrogen reduction experiments with amorphous 2H-MoS_2 and metallic 1 T-MoS_2 did not produce quantities of ammonia exceeding the background level,[12,21] while other studies report reasonable FEs and ammonia yields using FeS_2, Mo_2C, and Fe_3C, thereby labeling these materials as promising NRR catalysts.[22−24]

The electrochemical NRR field is plagued by questionable results, mainly due to the large impact of extraneous ammonia sources on experiments performed on a small scale. Ammonia stemming for other sources can erroneously be assigned to ammonia synthesized by the NRR, which can lead to false positives. Ammonia impurities can be minimized by a proper experiment design and can be identified by applying the right control experiments, such as argon and open-circuit blank tests and ultimately $^{15}N_2$-labeled experiments. Recently, nitrogen oxides have been identified as another source of contamination, as these species are more easily reduced to ammonia than dinitrogen in the NRR.[25] The majority of the recently published studies have applied blank tests, but performing quantitative $^{15}N_2$-labeled experiments and monitoring nitrogen oxide species are done sporadically.[25] As a consequence, a handful of research groups have tried to reproduce electrocatalysts initially labeled as promising, such as Fe, Bi, Au, VN, CoMo, Mo_2N, and MoS_2,[16,21,26−30] but discovered that the quantified ammonia must originate from sources other than the NRR. Here, we critically assess the electrocatalytic NRR activity of molybdenum and iron carbides, where more than 10 independent literature reports claim to observe superior or excellent catalytic performance.[23,24,31−38] In the present work, α-Mo_2C nanodots from Cheng et al. (reported as the most promising carbide catalyst) are reproduced and compared with α-Mo_2C nanoparticles as a benchmark.[23] Additionally, nanostructured θ-Fe_3C and χ-Fe_5C_2 are synthesized and examined for their NRR activity. A key aspect of this work is the implementation of a strict protocol, which is designed to minimize the level of extraneous contamination,[15,25] allowing genuine quantification of ammonia produced by the NRR.

2. EXPERIMENTAL SECTION

2.1. Materials. Materials and chemicals were purchased from Sigma Aldrich, if not indicated otherwise. Ultrapure water (Millipore Milli-Q IQ 7000) was used for catalyst synthesis, electrolyte preparation, and cleaning procedures. Concentrated sulfuric acid (95−98 wt % H_2SO_4, trace metal purity) was used for glassware acid cleaning and diluted for other purposes. High purity N_2, Ar, and H_2 (99.999%, Linde) were used for electrochemical experiments and material synthesis.

2.2. Molybdenum and Iron Carbide Synthesis.

2.2.1. Mo_2C Nanodot-Decorated Carbon Nanosheets. Mo_2C nanodots (Mo_2C NS) were synthesized by a molten-salt synthesis procedure as reported in detail elsewhere.[23] In short, a mixture of 1 mL of water and 4 mL of ethanol (96%, VWR) was mixed in a beaker and continuously heated and stirred on a hotplate. Once the mixture reached 70 °C, 0.4 g of bis(acetylacetonato)dioxomolybdenum(VI) and 0.14 g of sucrose (99.5%) were added. After the mixture turned green, an excess amount of sodium chloride (99.5%) was added until a green crystalline slurry was formed. The slurry was directly transferred to a ceramic boat and placed inside a tubular furnace (Blue, Lenton), where the specimen was heated to its carburization temperature under an Ar atmosphere (T_{carb} = 800 °C, heating rate = 5 °C min^{-1}), kept constant at this temperature for 2 h and the furnace cooled down to room temperature naturally. The resulting black catalyst/salt mixture was excessively rinsed with ultrapure water to remove the sodium chloride. The residue was filtrated (Durapore 100 nm, Merck) and dried in an oven at 80 °C overnight.

2.2.2. α-Mo_2C Nanoparticles. Gómez-Marín and Ticianelli reported a procedure for the synthesis of porous Mo_2C nanoparticles (Mo_2C NP) that was replicated here.[39] In a typical procedure, 0.15 g of Vulcan VC-72 (Cabot) was mixed with 0.51 g of MoO_3 (99.9%) in a beaker containing 30 mL of ethanol. The dispersion was heated to 60 °C overnight while continuously stirring to evaporate the ethanol completely. The powder was transferred to a ceramic boat for carburization inside a tubular furnace under 10 vol % H_2:Ar. The precursor was heated to 725 °C for 30 min with a slow heating rate (1 °C min^{-1}) and cooled down to room temperature.

2.2.3. Mesoporous Fe_3C. A combined hard-templating and carburization method developed by Kraupner and coworkers was used to create a mesoporous Fe_3C structure with a high surface area.[40] In brief, 0.5 g of $FeCl_3$ (99.9%) was dissolved in 1 g of 40 wt % SiO_2 in H_2O (Ludox AS40) in a borosilicate test tube. Additionally, 0.728 g of 4.5-dicyanoimidazole (99%) was added and stirred through the suspension and sonicated for 30 min to achieve a homogeneous yellow-colored thick slurry paste. The paste was transferred to a ceramic boat and carburized inside a tubular furnace at 700 °C (heating rate 2 °C min^{-1}) for 2 h under an Ar atmosphere and cooled down to room temperature.

2.2.4. χ-Fe_5C_2 Nanoparticles. The principle of thermodecomposition of $Fe(CO)_5$ is a common used strategy to synthesize iron carbides and is discussed in detail elsewhere.[41] A mixture of 0.2 g of polyvinylpiyrrolidone (PVP, 40000 g/mol) and 1 mL of $Fe(CO)_5$ (99.99%) was inserted in a homemade air-tight reactor consisting of Swagelock tubes and adapters (Figure S1). The reactor was purged with Ar at a flowrate of 20 mL min^{-1} for approximately 10 min to remove residual oxygen, and immediately afterward, all Swagelock adapters were closed. The reactor was positioned inside a

https://doi.org/10.1021/acscatal.2c04491
ACS Catal. 2023, 13, 1649−1661

muffle furnace programmed with T_{carb} at 300 °C (heating rate 2.3 °C min^{-1}) for a duration of 24 h.

2.3. Characterization. *2.3.1. X-ray Diffraction (XRD).* Samples were deposited on a Si510 zero background wafer and positioned inside a Bruker D8 Advance diffractometer in Bragg−Brentano geometry equipped with a graphite monochromator, a Vantec position sensitive detector, a variable divergence slit, and a 5 mm height scatter screen. Co Kα radiation (λ = 0.1789 nm) was used to avoid incident beam fluorescence effects on the Fe carbides. During each acquisition, steps with a size of 0.038° and 5 s per step were measured over a 10−110° 2θ range. Bruker DiffracSuite.EVA v6.0 was used to subtract the background, correct small displacements, and strip the Kα2 contribution from the patterns to enable crystallite size (D_{XRD}) estimation with the Scherrer equation (eq 1), where λ is the wavelength, and κ the shape factor taken as 1. Peak shapes were assumed Gaussian, and the full width at half-maximum, in this case β, was additionally corrected for instrumental line broadening effects.

$$D_{XRD} = \frac{\kappa\lambda}{\beta \cos\theta} \quad (1)$$

2.3.2. Mössbauer Spectroscopy. Transmission ^{57}Fe Mössbauer spectra were collected at room temperature with a conventional constant-acceleration spectrometer with a ^{57}Co(Rh) source. Velocity calibration was carried out using an α-Fe foil. The Mössbauer spectra were fitted using the Mosswinn 4.0 program.[42]

2.3.3. X-ray Photoelectron Spectroscopy (XPS). A Thermo Scientific Kα spectrometer with a monochromatic Al Kα excitation source was used to acquire X-ray photoemission spectroscopy (XPS) spectra. The base pressure inside the analysis chamber was about 2 × 10^9 mbar. HR-XPS spectra were recorded using a 400 μm spot size, 0.1 eV step size, and 50 eV pass energy (200 eV for survey). All spectra were charge-corrected to the C 1s adventitious carbon (284.8 eV). Subsurface layers were measured with a depth profile by argon ion etching (1000 eV) in between XPS measurements. The obtained XPS spectra were deconvoluted with CasaXPS v2.3 software.

2.3.4. Inductively Coupled Plasma Atomic Emission Spectroscopy (ICP-OES). The materials were dispersed in 35 vol % HNO_3 overnight to dissolve the carbides. The samples were further diluted with 3 vol % HNO_3 with an amount depending on the expected metal content. All ICP-OES measurements were performed on a SPECTRO ARCOS measured against an external calibration, with a typical detection limit of 10 ppb.

2.3.5. Scanning Electron Microscopy (SEM). Prior to analysis, the aluminum cylindrical sample holder was washed in isopropanol in an ultrasonic bath for approximately 2 min. An isopropanol based catalyst ink was drop-casted on the sample holder and positioned in a 25 mm working distance. The SEM measurements were executed on a Jeol JSM 6500F instrument at an acceleration voltage of 15 kV, coupled with an energy dispersed X-ray analysis detector (Ultradry, Thermo Scientific).

2.3.6. Transmission Electron Microscopy (TEM). A dispersion of catalyst and isopropanol was drop-casted on a TEM grid with a holey carbon film on a copper 400 mesh (EM-resolutions). All materials were analyzed with a JEOL JEM1400plus TEM at a 120 kV acceleration voltage using a single-tilt specimen holder. The TEM was equipped with a TVIPS TemCam-F416R high-resolution camera based on a custom designed CMOS architecture. ImageJ was used to estimate the particle size distribution.

2.4. Electrochemical Measurements. A Biologic VSP-300 potentiostat in combination with EC-Lab software was used for all electrochemical measurements. The uncompensated resistance (R_u) of the system (the resistance between the reference electrode (RE) and working electrode (WE)) was measured before each cyclic voltammetry (CV) and chronoamperometry (CA) measurement. R_u was determined with potentiostatic electrochemical impedance spectroscopy at open-circuit potential, with a frequency range between 200 kHz and 0.1 Hz. The distance between the origin and the first line intersection on the Z_{Real}-axes within the Nyquist plot represents R_u and was extracted by manual data fitting. Subsequently, the EC-Lab build-in IR compensation allowed 85% R_u compensation without adding to much distortion to the CV and CA results. Only for the CA experiments, the other 15% R_u was compensated after the measurement by using eq 2.

$$V_{100\%} = V_{85\%} + (iR_u)_{15\%} \quad (2)$$

A polyether ether ketone (PEEK) three-electrode cell design adapted from the Jaramillo group was used for all electrochemical experiments.[43] It consisted of two separate compartments that accommodate 5 mL of electrolyte and 3 mL of gas headspace. An additional plate was added to the overall cell design (Figure S2), which fixated the WE. A leak-free Ag/AgCl micro reference electrode (Innovative Instruments, LF-1-45) was used for potential control, wherein all potentials were recalculated versus the reversible hydrogen electrode scale following eq 3.

$$E_{RHE} = E_{Ag/AgCl} + E^0_{Ag/AgCl} + 0.059 \times pH \quad (3)$$

A Pt foil (50 × 50 × 0.025 mm, 99.99%, Mateck) functioned as the anode and was rinsed with water and flame annealed before each experiment. A fresh sheet of membrane (Celgard 3401) was used for every run, thereby preventing accumulation of NH_3. The WE was prepared by drop-casting 3 droplets of 10 μL of a freshly prepared catalyst ink (2 mg_{cat} ml^{-1}, 950 μL 2-propanol (98%, VWR) and 50 μL of Nafion 117-containing solution (5 wt %)) on a carbon paper disk (1 cm^2, Toray carbon paper, Aesar) with a loading of 0.06 mg cm^{-2} and stored under vacuum once prepared. The WE was soaked in a fresh 1 M KOH (99.95%), 0.1 M KOH, 0.5 M Li_2SO_4, or 0.05 M H_2SO_4 solution before it was fixated in the cell by a glassy carbon plate (25 × 25 × 1 mm, HTW). The back of the glassy carbon was taped with a Cu strip (AT528, 10 mm width, RS Components) and connected to the potentiostat wires. The catholyte was saturated by purging N_2 or Ar for 30 min before each experiment. After cyclic voltammetry and chronoamperometric measurements, aliquots of both catholyte and anolyte were collected with a syringe and transferred to several test tubes for further quantification.

2.5. Minimizing Effects of Impurities. Feed gas contamination in the form of NH_3 and NO_x in both high purity Ar and N_2 have been reported previously.[15,25] In order to remove residual contaminants, a certified commercial gas filter (Entegris GPUS35FHX) was installed upstream of the electrochemical cell (see Figure S3). The cell components were always acid cleaned with 10 vol % H_2SO_4 for at least 1 h and rinsed with ultrapure water prior to each experiment. Syringes, needles, pipet tips, and sample tubes were also

https://doi.org/10.1021/acscatal.2c04491
ACS Catal. 2023, 13, 1649−1661

excessively washed with ultrapure water and dried under Ar flow before use. A microporous membrane (Celgard 3401) with a gas repellent coating was selected as a more suitable separator compared to the more commonly used Nafion membrane to avoid accumulation of ammonia contaminations as was reported previously.[15,44,45] A downstream acidified liquid trap is often used to measure volatile ammonia that could potentially be present in the effluent gas. As NH_3 dissolves very well in aqueous electrolytes (~500 g/L), this suggests that low concentrations of NH_3 readily dissolves in the used electrolyte. This means that an acid trap is often redundant and can potentially be an extra source of contamination.[15] Therefore, we did not incorporate a downstream acidified trap in the experimental design.

Precursors and catalysts containing nitrogen species are potential sources of impurities and should be avoided.[28,30] The selection criteria for our catalyst synthesis procedures was mainly motivated by minimizing the use of N-containing precursors. The Mo_2C nanoparticles and Mo_2C nanodots do not contain N-based materials for the preparation, while the use of N−C compounds was unavoidable for the synthesis of iron carbide nanomaterials. The latter motivated us to use a catalyst loading of 0.06 mg·cm^{-2} to minimize the effects of the N−C precursor during the electrochemical experiments. We used a method adopted from Chen et al. to monitor impurities in our materials,[26] such as catalyst powders, membranes, carbon paper, and Pt foil. Strategies to effectively remove impurities will be discussed in a future study.[46]

Li-salts are notorious for containing trace levels of NO_x^- species as was previously reported by Li et al.[47] Therefore, Li_2SO_4 is suspected of having these labile N-species and the suggested thermal annealing step was implemented to remove trace impurities. For the annealing step, the as received Li_2SO_4 (99.5%) was transferred to a tubular furnace and thermally annealed at 800 °C for 4 h in Ar with a heating rate of 10 °C·min^{-1} before preparing a solution.

2.6. Ammonia and Nitrite Quantification. Ammonia was quantified by the Berthelot reaction.[48] In a routine analysis, a volume of 1.33 mL of either 1 M KOH, 0.1 M KOH, 0.5 M Li_2SO_4, or 0.05 M H_2SO_4 was neutralized with dilute concentrations of H_2SO_4 or KOH. Then, phenol nitroprusside and alkaline hypochlorite (0.2 wt % sodium hypochlorite in an alkaline solution) were both added in an amount equal to 25 vol % of the neutralized solution. The mixture was stirred thoroughly on a vortex shaker. After 30 min of incubation time, the solution color and its intensity differed from light green to dark blue with increasing NH_3 content. The samples were transferred to PMMA cuvettes (10 × 10 × 30 mm) for further analysis with the UV−Vis spectrophotometer (Hach DR6000). For constructing a calibration line, a series of six different concentrations of NH_4Cl (99.99%) in 1 M KOH, 0.1 M KOH, 0.5 M Li_2SO_4, and 0.05 M H_2SO_4 were prepared with respective concentrations of 0.01, 0.05, 0.1, 0.5, 1, and 2 ppm. The fitted calibration lines shown in Figure S4 were reproducible and resulted in the following linear relationships: $A_{1MKOH} = 0.5642C_{NH_3} - 0.0045$ with $R^2 = 0.9997$, $A_{0.1MKOH} = 0.7279C_{NH_3} - 0.001$ with $R^2 = 0.9999$, $A_{0.5MLi_2SO_4} = 0.7992C_{NH_3} - 0.0033$ with $R^2 = 0.9997$, $A_{0.05MH_2SO_4} = 0.6613C_{NH_3} - 0.00405$ with $R^2 = 0.9997$.

The concentration of NO_2^- was quantified by the photometric Griess test. A commercially available Griess reagent mixture was used with a detection range between 0.007 and 3.28 ppm NO_2^- (Spectroquant, Merck). Typically, a sample of 2 mL of 0.1 M KOH was neutralized with 168 μL of 0.5 M H_2SO_4. Subsequently, 30 mg of the Griess reagents were added and mixed with the solution with an incubation time of 10 min. Five different concentrations of 0.02, 0.05, 0.1, 0.5, 1 ppm KNO_2 in 0.1 M KOH were prepared to construct a calibration line with a perfect linear fit: $A = 0.8071C_{NO_2^-} - 0.0001$ and $R^2 = 1$ (Figure S5). The UV−Vis spectroscopic measurements to detect ammonia and NO_2^- were always performed versus a blank 0.1 M KOH electrolyte stock solution to exclude the influence of electrolyte background contaminations.

3. RESULTS AND DISCUSSION

3.1. Material Characterization. The X-ray diffraction patterns of Mo_2C NS, Mo_2C NP, Fe_3C and Fe_5C_2 are shown in Figure 1. The Mo_2C samples (Figure 1a) show three sharp

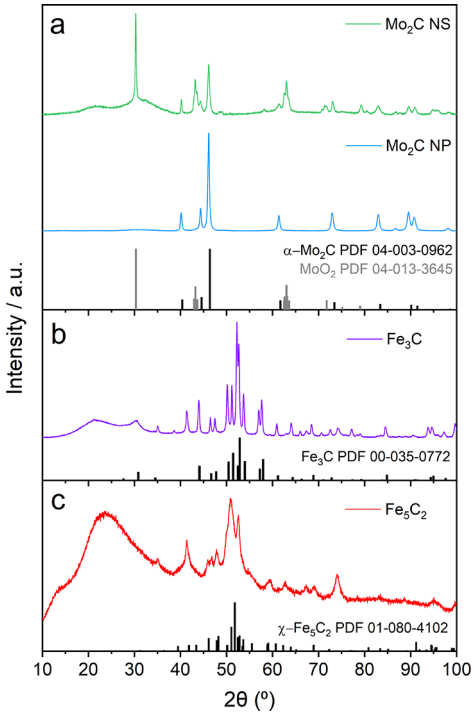

Figure 1. X-ray diffractions patterns of (a) Mo_2C NS (green) and Mo_2C NP (blue) with the α-Mo_2C (PDF 04-003-0962, black) and MoO_2 (PDF 04-013-3645, gray) reference patterns. The patterns in (b) and (c) represent Fe_3C (purple) and Fe_5C_2 (red) with the corresponding θ-Fe_3C (PDF 00-035-0772, black) and χ-Fe_5C_2 (PDF 01-080-4102, black) reference patterns.

peaks at 40.2, 44.3, and 46.1° that are identical to the reference spectrum of α-Mo_2C (PDF 04-003-0962). Three other peak features at 30.3, 43.2, and 63.0° suggest the existence of MoO_2 (PDF 04-013-3645) in the Mo_2C NS sample. This is most likely related to an incomplete carbothermal reduction of the molybdenum oxide precursor, which was not observed for the Mo_2C NP. The "hill-like" peak between 20 and 25° is typical for amorphous carbon and reflects its dominant presence in the Mo_2C NS, Fe_3C, and Fe_5C_2 samples.[49] The peaks between 45 and 60° in Figure 1b correspond to orthorhombic iron carbide (θ-Fe_3C, PDF 00-035-0772). The formation of other Fe oxidation states, such as reduced Fe (53.3°), Fe_3O_4 (41.3,

https://doi.org/10.1021/acscatal.2c04491
ACS Catal. 2023, 13, 1649−1661

35, and 74.2°), and Fe_2O_3 (38.6°) are inevitable by-products of the carburization process.[41,50] Also, small fractions of Fe_3O_4 (41.4° and 74°) were identified in Figure 1c after the thermal decomposition of $Fe(CO)_5$,[41] while the multiplet between 49 and 55° is very typical for χ-Fe_5C_2 (PDF 01-080-4102). The average crystallite size was calculated with the Scherrer equation (eq 1) and summarized in Table S1.

The fitted Mössbauer spectrum of the Fe_3C sample (Figure 2a) shows a sextuplet with an isomer shift (IS) of 0.19 mm s^{-1},

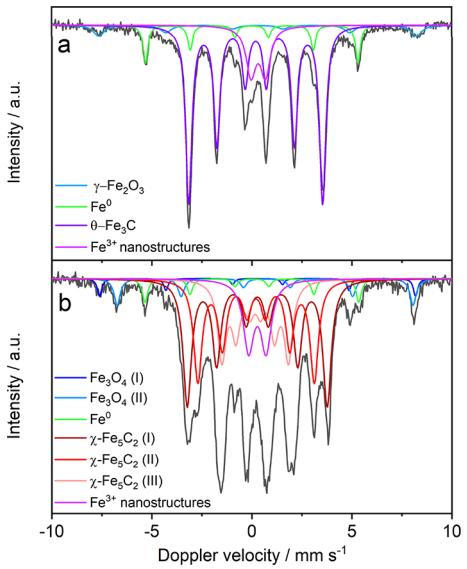

Figure 2. Room temperature transmission ^{57}Fe Mössbauer spectra in the (a) prepared Fe_3C sample with a large intensity sextet (purple) identified as θ-Fe_3C and (b) synthesized Fe_5C_2 powder with three intense sextets of χ-Fe_5C_2 (I maroon, II red, III salmon).

and a hyperfine field of 20.8 T. θ-Fe_3C is identified as the major spectral contributor (67%).[51] Additionally, a metallic Fe sextuplet (IS = −0.004 mm s^{-1}, 33 T) was clearly observed and is in agreement with the sharp peak at 53.3° in the Fe_3C diffractogram. A doublet indicates a quadrupole peak splitting, which means the absence of magnetic field spin coupling. This indicates the presence of (super)paramagnetic Fe^{3+} nanostructures. It is difficult to allocate the specific Fe^{3+} phase, as multiple subdoublets can be superimposed in one doublet.[52] However, the low intensity XRD peaks of Fe_2O_3 suggests that the doublet contains mostly nanostructured Fe_3O_4. The presumably low quantities of Fe_2O_3 are covered by a sextet (IS = 0.31 mm s^{-1}, 49.3 T); therefore, it is unlikely that Fe_2O_3 has a spectral contribution in the doublet. Three sextuplets (IS = 0.27, 0.21, and 0.16 mm s^{-1} with B_{hyp} = 21.7, 18.1, and 10.3 T) covered 78% of the spectral area in Figure 2b, which were attributed to the three iron lattice sites in the Fe_5C_2 crystal structure.[53,54] Fe_3O_4 has a small spectral contribution located in the outer spectrum with an octahedral (IS = 0.28 mm s^{-1}, 49.1 T) and a tetrahedral site (IS = 0.71 mm s^{-1}, 46 T).[55] Fe_2O_3 was not identified in the Fe_5C_2 diffractrogram, which again suggests that the doublet is nanostructured Fe_3O_4. In conclusion, the Mössbauer data confirms the synthesis of the intended Fe_3C and Fe_5C_2 compounds with limited amounts of iron and iron oxide species. The remainder of the Mössbauer data is summarized in Table S2.

Mössbauer spectroscopy and XRD give information about the bulk phase of the material. XPS is surface sensitive and gives information regarding the surface phase and composition. The Mo_2C XPS survey scans (Figure S6a,b) contain peaks of Mo 3d, Mo 3p, C 1s and O 1s, from which the high-resolution scans of the Mo 3d photoelectrons (Figure 3a,b) were

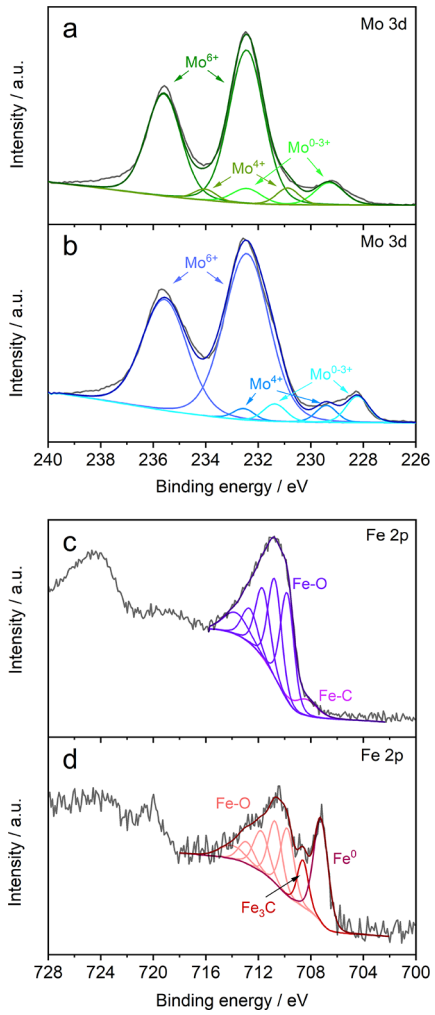

Figure 3. X-ray photoelectron spectroscopy Mo 3d and Fe 2p spectra with deconvoluted peaks in (a) Mo_2C NS (green) and (b) Mo_2C NP (blue), (c) orthorhombic Fe_3C (purple), and (d) Fe_5C_2 (red).

deconvoluted to identify different Mo oxidation states. The Mo 3d orbital has a spin−orbit Mo $3d_{5/2}$-Mo $3d_{3/2}$ doublet with a 3/2 peak intensity ratio that is separated by a binding energy of 3.15 eV. The full width at half-maximum (FWHM) was kept constant for each doublet during the deconvolution process. It is often ambiguous to assign an oxidation state to Mo_2C; therefore, it is often denoted in an aggregated term as Mo^{0-3+}.[56] The presence of Mo_2C surface bonded species was confirmed by the small Mo $3d_{5/2}$ peaks at 229.3 and 228.2 eV for both Mo_2C NS and Mo_2C NP, respectively.[34,57] Other peaks at binding energies 232.5 and 235.5 eV for both Mo-carbide materials are identified as MoO_3 and must be solely present in the thin surface layers as MoO_3 was not identified in the diffractograms. These spontaneously formed metal oxide surface layers are inevitable due to exposure to ambient air. Post-mortem XPS analyses confirmed that the majority of the surface layer was Mo_2C.[23,58] This suggests that the Mo-oxide species are reduced during electrochemical reduction. Moreover, it is expected that the trans-passive Mo-oxide layers are

https://doi.org/10.1021/acscatal.2c04491
ACS Catal. 2023, 13, 1649−1661

not stable in alkaline conditions and form soluble MoO_4^{2-} even at moderate reduction potentials.[59,60]

The Fe $2p^{3/2}$ peak was used to identify different Fe oxidation states. The broad peak between 714 and 709 eV contains a complex convolution of multiple subpentuplets of Fe_2O_3, Fe_3O_4, and FeOOH species, which all overlap in this region. We fitted one pentuplet as a general Fe-oxide term as indicated in Figure 3c,d by taking XPS reference data such as FWHM, relative peak area, and binding energies from Biesinger et al.[61] For iron carbide, the majority of the surface is covered with a thin Fe-oxide layer. According to the Pourbaix diagram for Fe, this oxide-layer is reduced by applying mild reduction potentials.[62] The presence of a single peak at 708.4 eV for Fe_3C and 708.6 eV for Fe_5C_2 is identified as the Fe carbide phase. Only Fe_5C_2 has an additional sharp metallic Fe peak at 707.2 eV. The low signal-to-noise ratio for the Fe_5C_2 Fe 2p spectra indicates a low Fe quantity (<1 at%), which is also reflected in a low intensity Fe oxide peak in the O 1s spectra (Figure S7e). From a depth profiling test (Figure S8), it becomes clear that the Fe 2p signal increases with a longer etching time, while the intensities of the O 1s and N 1s spectra decreases. This indicates that the top surface layer is covered with adventitious species due to atmospheric exposure.

The elemental Mo and Fe content in all metal carbides were analyzed by ICP-OES and are summarized in Table S3. The ICP-OES results revealed that the bulk concentrations of Mo and Fe are significantly higher with respect to the surface concentrations estimated by XPS. This suggests that the surface adsorption of advantageous species by air exposure is not only observed for Fe_5C_2 but also for the other metal carbides.

The Mo_2C NS are clearly visible in Figure 4a,e and confirm a successful synthesis. TEM imaging (Figure S9a) reveals that a relatively large proportion of the sample consists of undecorated carbon nanosheets. This explains why the majority of the surface composition, analyzed by XPS, is predominantly carbon (Table S4). The existence of Mo_2C nanodots (<20 nm), as proposed by Wang and coworkers, was not observed in our TEM analysis.[23] Despite the magnification limitations of the low-resolution TEM, distinguished nanoparticles up to 5−10 nm were detectable in other metal carbide samples, indicating that Mo_2C nanodots of the order 10−20 nm should be visible. In Figure 4e and Figure S9b, regions with a higher contrast indicate a layer of aggregated Mo_2C, with an average crystallite size (D_{XRD}) of 35 nm. The SEM−EDX results (Figures S10 and S11) support this observation and show that the carbon sheet is indeed covered with a nanocrystalline layer of Mo_2C.

The successful synthesis of Mo_2C NP on a carbon support was confirmed by TEM (Figure 4f and Figure S12). The particle size, D_{TEM}, was distributed between 10 and 50 nm, which is in agreement with the average crystallite size (D_{XRD} = 21 nm). The SEM images in Figure 4b and Figure S13 show a mesoporous morphology with a large surface area. The overall Mo_2C surface distribution is homogeneous as was confirmed by the SEM−EDX mapping (Figure S14). The carbon precursor in combination with the inert SiO_2 nanoparticles stimulates the spherical growth of nanosized Fe_3C particles and prevents it from forming larger aggregates. Most Fe_3C particles were between 40 and 60 nm. The Fe_3C sample contained nanosized hollow features as visible in Figure 4c,g and confirmed the successful removal of SiO_2 during the 1 M KOH treatment. The absence of the SiO_2 nanoparticles after the treatment was further supported by Fourier transform infrared spectroscopy (Figure S15).

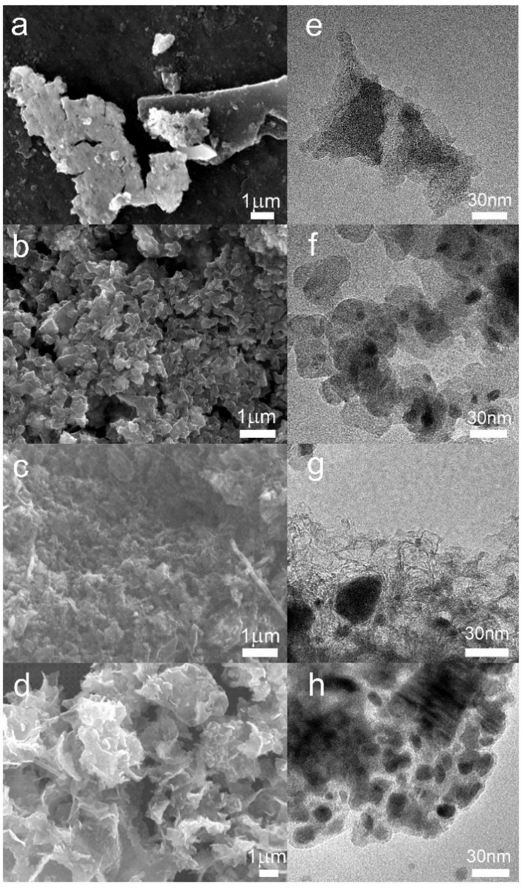

Figure 4. Scanning and transmission electron micrographs of (a, e) Mo_2C NS, (b, f) Mo_2C NP on a carbon support, (c, g) Fe_3C, and (d, h) Fe_5C_2.

Small and isolated Fe_5C_2 spherical nanoparticles with a narrow size distribution are observed in Figure 4d and Figure S16 (D_{TEM} is 5−35 nm and D_{XRD} is 11 nm). This highlights that PVP successfully stabilizes the nanoparticles from agglomeration during the carbothermal reduction of $Fe(CO)_5$. The material has a microporous structure (Figure S17b) with a high surface area because of the polymeric nature of the support. In contrast to the low Fe content measured in the first ∼10 nm-thick surface layer, well distributed and significant Fe concentrations were detected in the bulk surface layers (∼1 μm) by SEM−EDX mapping (Figure S18), which supports the XPS depth profiling and ICP-OES results (Figure S8).

3.2. Electrochemical Characterization. The current-potential (I−V) relationship of each material was investigated by executing multiple CV cycles at a scan rate of 20 $mV{\cdot}s^{-1}$ in a N_2 presaturated electrolyte to estimate the onset potential and an expected potential window for the NRR. A possible pH dependency on the Mo_2C activity of the NRR was investigated by executing CV in 0.05 M H_2SO_4 (pH = 1), 0.5 M Li_2SO_4 (pH = 8.3), 0.1 M KOH (pH 13), and 1 M KOH (pH 14). The stability of Fe-carbides in acidic-to-neutral conditions is low as the material tends to dissolve.[63] Therefore, we decided to only use 0.1 M and 1 M KOH for the evaluation of the Fe-carbides. Mo_2C is generally stable in both acidic and alkaline environments, allowing CV measurements in all electrolytes.[58,64] The uncompensated resistance (R_u), measured

https://doi.org/10.1021/acscatal.2c04491
ACS Catal. 2023, 13, 1649−1661

with open-circuit electrochemical impedance spectroscopy was consistent for each material tested and ranged between 25 and 30 Ω for 0.1 M KOH, 3 and 4 Ω for 1 M KOH, 12 and 13 Ω for 0.5 M Li_2SO_4, and 24 Ω for 0.05 M H_2SO_4 (Figure S19). These quantities for R_u are below the acceptable range of the R_u compensator used for all electrochemical measurements.

Figure 5 shows that all metal carbide $I-V$ relationships in acidic, neutral, and alkaline conditions display an increase in current density at increasingly more negative potentials, characteristic for an HER $I-V$ profile. Other distinctive reduction peaks that might be identified as the NRR were not observed in the voltammetry measurements. In addition to this, there was no indication of a metal oxide reduction peak within the examined potential window, which suggests that the metal oxide surface layer is removed immediately. Mo_2C NP reaches higher current densities compared to Mo_2C NS at all pH values, which could be explained by a larger electrochemical surface area due to the mesoporous structure of Mo_2C NP. Another explanation might be the higher Mo_2C loading content in Mo_2C NP, since the ICP-OES analysis resulted in a higher concentration of elemental Mo in Mo_2C NP.

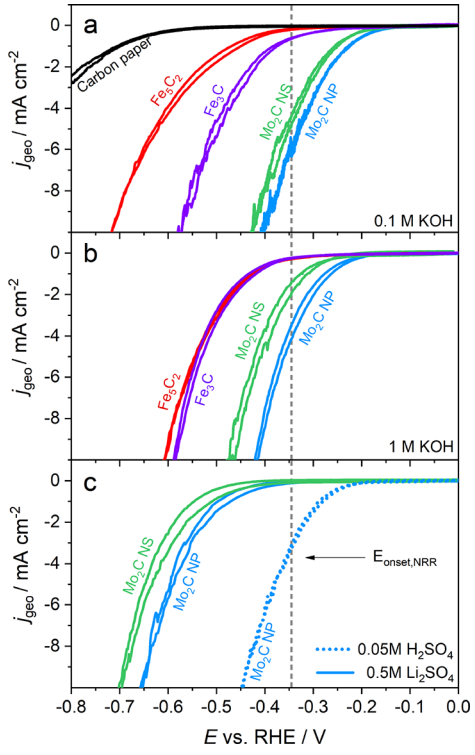

Figure 5. Cyclic voltammograms (6th cycle) at 20 mV·s^{-1} for Mo_2C NS (green), Mo_2C NP (blue), Fe_3C (purple), Fe_5C_2 (red), and carbon paper (black) in (a) 0.1 M KOH, (b) 1 M KOH, (c) 0.5 M Li_2SO_4, and 0.05 M H_2SO_4. The gray dotted line at −0.345 V vs RHE represents the theoretically estimated onset potential for the NRR.

The onset potential is used to indicate the minimum activation potential of a redox reaction in cyclic voltammograms.[65] A theoretical approximation of the NRR onset potential in alkaline media can be calculated using the equilibrium potential and the activation overpotential. First-principles density functional theory calculations suggest that the minimum overpotential for the NRR is approximately −0.4 V, due to scaling relationships between intermediates.[2,66] The NRR equilibrium potential was calculated by equilibrium thermodynamics and is 0.054 V vs RHE, which results in a minimum required onset potential ($E_{onset,\ NRR}$) of −0.35 V vs RHE. Here, we estimated the experimental E_{onset} for different pH values by plotting the first derivative of the voltammogram (dj/dE) versus the applied potential (Figure S20). The lift-off point where the slope of the dj/dE curve starts to increase is set as the E_{onset}.

For 0.1 M and 1 M KOH, we do not see clear evidence for an alkaline pH effect for Mo_2C materials as both Mo_2C NP and NS have a similar $I-V$ curve at both KOH concentrations. The onset potential for Mo_2C NP of −0.11 V vs RHE is similar for both electrolytes and is in agreement with earlier observations.[64] Moreover, the onset potentials for Fe_3C and Fe_5C_2 are also similar and varied between −0.22 and −0.23 V vs RHE for both 0.1 M and 1 M KOH. The $I-V$ relationship in Figure 5c for Mo_2C in 0.5 M Li_2SO_4 is remarkably different showing a more negative onset potential of −0.28 V vs RHE and −0.32 V vs RHE for Mo_2C NP and NS, respectively. As a consequence, the activation overpotential at −10 mA·cm^{-2} for Mo_2C NP is −0.25 V lower than in alkaline conditions, which can be related to the low availability of either protons or hydroxide ions. At acidic conditions (pH = 1), Mo_2C NP displays a similar $I-V$ relationship with respect to alkaline conditions, which highlights the unique properties of Mo_2C showing similar catalytic activity in both acidic and alkaline conditions.[64] However, the onset potential is slightly more negative (−0.17 V vs RHE), indicating that the catalyst is more active in alkaline conditions.

E_{onset} for Mo_2C is above the theoretically estimated threshold in both acidic and alkaline pH, where the current density $E_{onset,NRR}$ is roughly −4 mA·cm^{-2} for Mo_2C NP. From this analysis, it is unlikely that the NRR is a dominant contributor to the $I-V$ profile of Mo_2C because the HER kinetics are more facile in these conditions. Interestingly, E_{onset} for Mo_2C in 0.5 M Li_2SO_4 is below $E_{onset,NRR}$ and suggests that operating at near-neutral conditions might be ideal for the NRR. It is important to note that Cheng and coworkers reported high NH_3 yields with Mo_2C NS using the same electrolyte.[23] For Fe_3C and Fe_5C_2, the majority of the $I-V$ profile exceeds $E_{onset,NRR}$, suggesting that both iron carbides might be promising catalysts for the NRR.

The NRR activity of the metal carbides was qualitatively screened by measuring the ammonia concentration after executing 40 scans of cyclic voltammetry with a scan rate of 20 mV s^{-1}. The results are summarized in Figure S21 and show that NH_3 concentrations for Mo_2C in acidic-neutral pH is close to the detection limit <30 ppb, while levels up to 100 ppb were observed in alkaline conditions. Operating at alkaline conditions is therefore more beneficial for studying the NRR, and subsequently, the main electrochemical experiments herein were performed in alkaline conditions.

To ultimately verify Mo- and Fe-carbides as conceivable NRR catalysts, a series of 2 h chronoamperometry (CA) measurements were performed at five different potentials in a N_2-saturated 0.1 M KOH electrolyte. The current densities for the metal carbides are stable in alkaline conditions as illustrated in Figure S22. As a comparison, two additional CA measurements in Ar-saturated electrolytes were performed with Mo_2C, which gave slightly higher current densities for two potentials. The difference in current density is however rather small and can be caused by slight variations in the experiments. This observation was also made elsewhere,[28] questioning the

https://doi.org/10.1021/acscatal.2c04491
ACS Catal. 2023, 13, 1649−1661

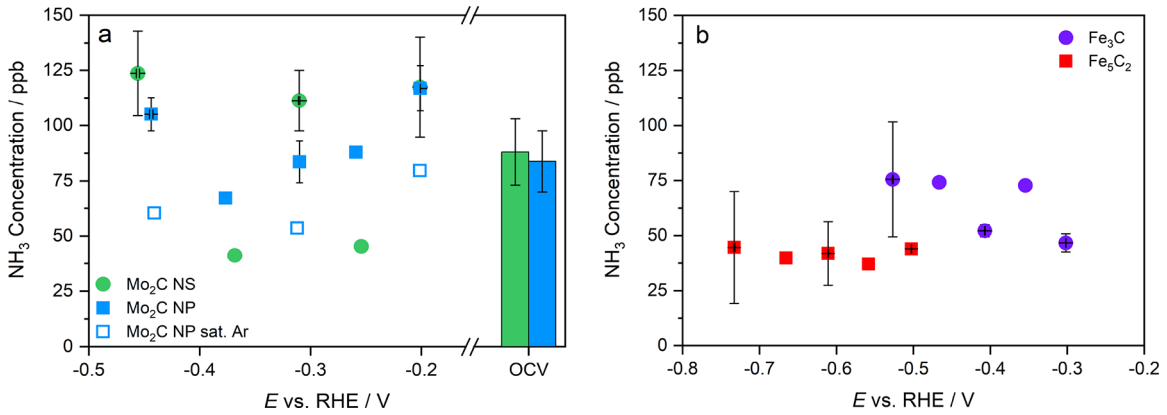

Figure 6. NH_3 concentration measured from the electrolyte after two hour CA experiments in 0.1 M KOH. (a) Mo_2C NS (green, spherical) and Mo_2C NP in N_2 (blue, rectangular) and Ar (open rectangular). (b) Fe_3C (purple, spherical) and Fe_5C_2 (red, rectangular). The data points with the error bars were done in duplicates.

reliability of N_2 vs Ar voltammetry and CA experiments as an initial indicator for successful dinitrogen reduction.

3.3. NRR Measurements. CA measurements were used to further assess the activity toward the NRR. After each CA, aliquots of both catholyte and anolyte were taken from the cell for further quantification of NH_3 and NO_2^-. The amount of quantified NH_3 after each experiment varied between 37 and 123 ppb with no particular trend linking ammonia concentration and applied potential over time. A 2 h open circuit potential (OCV) test with a N_2-saturated electrolyte was used to obtain insights on the amount of impurities coming from either the feed gas stream or surface adsorbed species inside the cell. The OCV results for Mo_2C reveal a similar NH_3 concentration as obtained with the chronoamperometry experiments. The impact of feed gas impurities can be excluded due to the installed certified gas filter (<100 ppt) in front of the cell. It is more likely that adsorbed NH_3 in the cell components is released during the OCV experiments and inevitably during the NRR measurements. Long term CA experiments with an Ar-saturated electrolyte are useful to study the possible release of N-impurities from the catalyst and other cell components exposed to the electrolyte under electrochemical conditions. For Mo_2C, three CA experiments with Ar-saturated electrolyte at −0.20, −0.31, and −0.44 V vs RHE resulted in a somewhat lower NH_3 content (80, 53, and 60 ppb) compared to experiments with N_2-saturated electrolytes. Again, it is deemed unlikely that purified Ar (and N_2) introduces feed gas impurities. Therefore, this observation suggests that the Ar gas flowing through the electrolyte stripped a small part of the dissolved NH_3 from the electrolyte. Nevertheless, both the N_2 OCV and Ar CA experiments indicate that the majority of the quantified NH_3 is not from the NRR but originates from contaminations. Additional control experiments with $^{15}N_2$-labeled gas were not performed since the observed NH_3 concentrations were below or approximating the background level.

Small quantities of NO_2^- were detected after all CA experiments, suggesting that a part of the quantified NH_3 potentially stems from NO_x reduction. Jiao and coworkers observed that the electrochemical reduction of NO_x forms multiple N-products, such as ammonia, hydroxylamine, N_2, and N_2O depending on the transition metal.[67] Pt is more selective toward NH_3, which was also supported by Koper and coworkers who made a similar observation for NO_3^- electroreduction on Pt.[68] Mo_2C has similar noble metal-like properties as platinum;[69] therefore, it is reasonable to assume that NO_x species are reduced to ammonia at the investigated potentials. Fe_3C is also an efficient nitrate reduction electrocatalyst, where a previous study reported faradaic efficiencies (FE) higher than 90% to NH_3 at moderate reduction potentials.[70]

Despite the thorough cleaning efforts for every part of the cell, a well-established background level of both NH_3 and NO_2^- was always observed after each experiment. We decided to analyze the removal efficiencies of our cleaning methods (elaborated in the caption of Figure S23) and found that NH_3 was sufficiently removed by simply rinsing with water. Surprisingly, significant quantities of released NO_2^- were detected that originated from the Celgard 3401 membrane, carbon paper, and Pt foil. This is a valuable observation, as two previous studies advised substituting the Nafion membrane with a microporous Celgard membrane to reduce NH_3 contaminations.[15,45] Our results indicate that NO_2^- is not only a surface adsorbed species but is also present in the inner membrane and carbon paper structure and is problematic to remove. Generally, the amount of released NO_2^- depends mainly on the exposed surface area, meaning that it can be lowered significantly by optimizing the cell design. Investigating the origin of the observed NO_x impurities is out of the scope of the present work and will be addressed in an upcoming study.[46]

3.4. Literature Comparison. Previous studies using Mo- and Fe-carbides as NRR electrocatalysts are shown in a comparative overview (Figure 7a), including our own observations. It becomes clear that both our Fe_3C and Fe_5C_2 quantified NH_3 yields are within the NH_3 background level. The Mo_2C catalysts exceed this threshold slightly, but with a significant NO_x background, it becomes unlikely that any nitrogen reduction to NH_3 occurred. The study of Cheng and coworkers outperformed our Mo_2C NS, observing a 240 times higher NH_3 yield.[23] This motivated us to execute a direct comparison by increasing the catalyst loading to 3 $mg \cdot cm^{-2}$ and using 0.5 M Li_2SO_4. The chronoamperometry measurements were comparable, but our NH_3 concentrations were below 100 ppb and close to the earlier defined background level as displayed in Figure 6. This is additional proof that Mo_2C cannot be perceived as a promising NRR catalyst.

https://doi.org/10.1021/acscatal.2c04491
ACS Catal. 2023, 13, 1649−1661

The majority of the earlier published literature observed orders of magnitude higher yields and FEs compared to this work. Firstly, all the literature studies shown in the overview did not quantify or consider NO_x as an influential factor on their measured NH_3 content. Secondly, the impurities in the feed gas stream were not removed by the installment of a certified gas filter. This is especially important when performing $^{15}N_2$-isotope labeled experiments as traces of ^{15}N-labeled impurities ($^{15}NH_3$ and $^{15}NO_x$) have been identified in several $^{15}N_2$-gas bottles.[15,25,71,72] Before using Li-based electrolytes for NRR experiments, Li-salts must be thermally annealed at 800 °C under inert conditions to remove trace levels (>1 ppm) of NO_x^- impurities.[47] We followed this procedure, while others, including Cheng et al., did not consider this extraneous source of impurities, and this might be one of the main factors contributing to their high NH_3 yields.[23,31,36] As final point, the Nafion membrane commonly applied in these studies is known for the uptake and release of NH_3 during electrochemical experiments.[15] Substituting the Nafion membrane with another membrane is not straightforward as we detected a significant amount of NO_2^- in the microporous membranes (Celgard 3401), but selecting a suitable treatment method is advised.[73]

Control experiments become even more essential when catalysts have a high N-content, such as metal nitrides, N-doped supports, or leftover NO_x/NH_3 traces from the catalyst synthesis. Evidence was found that for catalysts with a high N content, such as VN and Nb_4N_5, the decomposition of the N-atomic lattice in acidic media released significant amounts of NH_4^+ during the initial stages of the electrochemical experiment.[28] Similar observations were also reported for Mo_2N.[30] Additionally, several commercially available metal oxide powders, such as Fe_2O_3 and Bi_2O_3, released a large amount of NO_x impurities. This eventually led to the retraction of a study, as it was proven that the origin of observed NH_3 was from NO_x reduction and not the NRR.[26,74] Therefore, we decided to analyze the N-content of all four materials by XPS and UV−Vis spectroscopy (method described in the SI). The N 1s spectra of Mo_2C could not be identified because of overlapping peak features with the Mo 3p orbital. Nevertheless, the absence of N KLL Auger peaks in both Mo_2C NS and NP XPS surveys (Figure S6a,b) indicate that the N-content might be negligible. Figure S7c,f shows two distinct N 1s peaks for Fe_3C (398.3 and 399.9 eV) and Fe_5C_2 (398.9 and 400.1 eV), suggesting pyridinic N−C and pyrrolic N−C bonds from the precursor (4.5-dicyanoimidazole and PVP).[75] Nevertheless, the samples were exposed to air before XPS analysis, indicating that the peaks could be also from adventitious N species, such as $-NH_2$, which have similar binding energies.[75−77] It is therefore challenging to assign these peaks to a specific N-functional group. From the spectrophotometric analysis (Figure S25), directly performed after the material synthesis, it becomes clear that NH_3 impurities from an unidentifiable source were present in all catalysts (Mo_2C NS = 8.9 $\mu mol_{NH3}\ g_{cat}^{-1}$, Mo_2C NP = 16.5 $\mu mol_{NH3}\ g_{cat}^{-1}$, Fe_3C = 21.9 $\mu mol_{NH3}\ g_{cat}^{-1}$, Fe_5C_2 = 4.5 $\mu mol_{NH3}\ g_{cat}^{-1}$). This effect was suppressed by using a low catalyst loading (0.06 mg) for each experiment. In the case of the most contaminated sample, the expected release of NH_3 from 0.06 mg Fe_3C is limited to a negligible 1.3 nmol. Nevertheless, the NRR measurements performed with 3 mg Mo_2C NS did not result in an increase in the NH_3 concentration. It remains unlikely that impurities in the catalyst resulted in exceptionally high NH_3 yield reported by Cheng et al.[23] This suggests that other factors lead to their positive result.

The NH_3 partial current density, j_{NH_3}, is a useful performance indicator, wherein cases with j_{NH_3} smaller than 100 $\mu A\ cm^{-1}$ are too low to be promising. From a back-of-the-envelope calculation, we estimated that the NH_3 concentration at j_{NH_3}=100 $\mu A\ cm^{-1}$ is in the 1 ppm order of magnitude range assuming typical parameters, such as A_{WE} = 1 cm^2, $V_{catholyte}$ = 20 mL, and t_{CP} = 1 h. These levels of NH_3 can easily be reached when the earlier mentioned sources of contamination are not identified or even considered. This has implications on the reliability and usefulness of reporting the FE, wherein the focus should be initially on j_{NH_3} or the NH_3 yield rate. From Figure 7b, it becomes clear that most literature studies did not exceed 100 $\mu A\ cm^{-1}$, while a FE > 20% was reported (see Table S4). Therefore, we suggest that future publications explicitly report the NH_3 partial current density as the main catalyst performance indicator.

Interestingly, the role of metal carbides is also under debate for hydrazine oxidation.[78] Fe−N−C catalysts are common

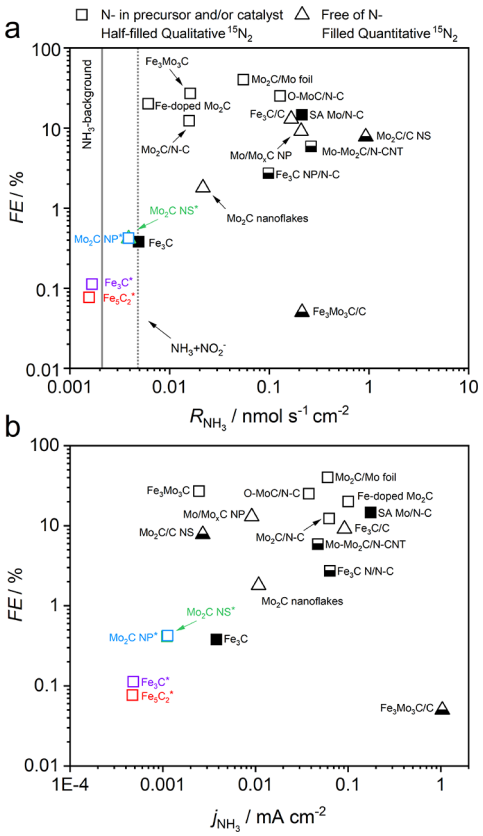

Figure 7. Literature overview of recently published NRR studies using Mo- and Fe-carbides as electrocatalysts differentiated by either high N-source in the support or used during synthesis (square) and free of N-source (triangular). The symbols are filled in case of quantitative $^{15}N_2$-labeled experiments and half-filled if analyzed qualitatively. Our own results are included as Mo_2C NS* (green), Mo_2C NP* (blue), Fe_3C* (purple), and Fe_5C_2* (red). (a) Faradaic efficiency vs NH_3 yield with thick line (gray) indicates the estimated NH_3 background level and the dotted line presents a hypothetical background level including the measured NO_2^- from Figure S24. (b) Faradaic efficiency vs j_{NH_3}. More details regarding the literature studies included in the figure can be found in Table S4.

https://doi.org/10.1021/acscatal.2c04491
ACS Catal. 2023, 13, 1649−1661

used catalysts for this reaction and contain iron carbides because of the high temperature pyrolysis required for the synthesis. Early studies claimed that Fe_3C plays an active role in the reaction,[79,80] while a recent study revealed the true role of Fe_3C by executing a rigorous comparison study between Fe−N−C materials with different amounts of Fe_3C.[78] This approach led to the conclusion that Fe_3C is mostly inactive for hydrazine oxidation, and should be removed by nonoxidizing acid solutions. This is yet another example of how a rigorous and well-designed experimental procedure can aid in clarifying the activity of electrocatalysts for reactions in the nitrogen cycle.

4. CONCLUSIONS

Nanostructured molybdenum carbide and iron carbide were reported earlier as promising electrochemical nitrogen reduction catalysts. In this study, the NRR activity of both molybdenum and iron carbide materials were reassessed with the implementation of a strict experimental protocol that allowed us to reduce the effects of extraneous impurities to a bare minimum and identify false positives. The successful synthesis of nanostructured Mo_2C, Fe_3C, and Fe_5C_2 was confirmed by X-ray diffraction, scanning and transmission electron microscopy, and X-ray photoelectron and Mössbauer spectroscopy. The current−potential relationship of the metal carbides is characteristic for the HER, where the current increases with increasing negative overpotential. Moreover, specific reduction peaks that could be related to the NRR were not identified. NH_3 quantification was done after 40 scans of cyclic voltammetry, where we indeed measured NH_3 (50−100 ppb) for both Mo_2C and Fe_5C_2 in alkaline conditions. To further assess the NRR catalytic activity of molybdenum and iron carbides, we performed a series of 2 h chronoamperometry measurements at different potentials in N_2-saturated 0.1 M KOH. For Mo_2C NP and NS, the NH_3 concentration was between 41 and 124 ppb, exceeding the NH_3 background level (84−88 ppb) for potentials at −0.2, −0.31, and −0.46 V vs RHE. We noticed that the yield earlier reported by Cheng et al. was considerable higher than measured with our Mo_2C NS.[23] A direct comparison by performing chronoamperometry experiments with an increased loading (3 mg·cm^{-2}) and 0.5 Li_2SO_4 did not result in elevated NH_3 concentrations. This is additional proof that Mo_2C cannot be conceived as a promising NRR catalyst. The NO_x content after the NRR, Ar, and OCV blank tests revealed NO_2^- concentrations in the same order of magnitude (55−122 ppb). This implies that NH_3 arises from NO_2^- reduction and not from the NRR. These NO_2^- impurities originated from the Celgard membrane, since we found that the membrane, even after rinsing excessively with water, released a considerable amount of NO_2^- impurities (109 ± 31 ppb). This emphasizes the importance of NO_x monitoring, which is often overlooked in the literature and might result in a false positive. The quantified NH_3 from the iron carbide catalysts did not exceed the NH_3 background level, indicating that these materials are not active for the NRR. With our experimental approach, we succeeded in establishing a minimized and reproducible background level that allowed us to critically assess promising NRR catalysts. We believe that our methods and detailed analysis will equip researchers entering the field with clear guidelines to perform NRR experiments in a more reliable manner.

■ ASSOCIATED CONTENT

Supporting Information

The Supporting Information is available free of charge at https://pubs.acs.org/doi/10.1021/acscatal.2c04491.

Additional information on the experimental setup, UV−vis calibration curves, XRD analysis, Mössbauer data, XPS, SEM−EDX, TEM, ICP-OES, FT-IR, electrochemical data, impurity assessment, and a literature summary (PDF)

■ AUTHOR INFORMATION

Corresponding Author

Ruud Kortlever − *Large Scale Energy Storage, Process and Energy Department, Faculty of Mechanical, Maritime and Materials Engineering, Delft University of Technology, Delft 2628 CB, The Netherlands*; orcid.org/0000-0001-9412-7480; Email: R.Kortlever@tudelft.nl

Authors

Boaz Izelaar − *Large Scale Energy Storage, Process and Energy Department, Faculty of Mechanical, Maritime and Materials Engineering, Delft University of Technology, Delft 2628 CB, The Netherlands*

Davide Ripepi − *Materials for Energy Conversion and Storage, Chemical Engineering Department, Faculty of Applied Sciences, Delft University of Technology, Delft 2629 HZ, The Netherlands*; orcid.org/0000-0001-7488-6690

Simone Asperti − *Large Scale Energy Storage, Process and Energy Department, Faculty of Mechanical, Maritime and Materials Engineering, Delft University of Technology, Delft 2628 CB, The Netherlands*

A. Iulian Dugulan − *Radiation Science and Technology Department, Faculty of Applied Sciences, Delft University of Technology, Delft 2629 HZ, The Netherlands*

Ruud W.A. Hendrikx − *Surface and Interface Engineering, Materials Science and Engineering Department, Faculty of Mechanical, Maritime and Materials Engineering, Delft University of Technology, Delft 2628 CB, The Netherlands*

Amarante J. Böttger − *Surface and Interface Engineering, Materials Science and Engineering Department, Faculty of Mechanical, Maritime and Materials Engineering, Delft University of Technology, Delft 2628 CB, The Netherlands*

Fokko M. Mulder − *Materials for Energy Conversion and Storage, Chemical Engineering Department, Faculty of Applied Sciences, Delft University of Technology, Delft 2629 HZ, The Netherlands*; orcid.org/0000-0003-0526-7081

Complete contact information is available at: https://pubs.acs.org/10.1021/acscatal.2c04491

Notes

The authors declare no competing financial interest.

■ ACKNOWLEDGMENTS

The authors would like to thank Hans Brouwer for his valuable assistance during the high-temperature carburization experiments and Michel van den Brink for performing the ICP-OES measurements. This work is part of the Nitrogen Activation and Ammonia Oxidation project within the Electron to Chemical Bonds consortium with project number P17-08, which is financed by The Netherlands Organisation for Scientific Research (NWO) and affiliated industrial partners.

REFERENCES

(1) MacLeod, K. C.; Holland, P. L. Recent developments in the homogeneous reduction of dinitrogen by molybdenum and iron. *Nat. Chem.* **2013**, *5*, 559−565.

(2) Van Der Ham, C. J. M.; Koper, M. T. M.; Hetterscheid, D. G. H. Challenges in reduction of dinitrogen by proton and electron transfer. *Chem. Soc. Rev.* **2014**, *43*, 5183−5191.

(3) Rösch, B.; Gentner, T. X.; Langer, J.; Färber, C.; Eyselein, J.; Zhao, L.; Ding, C.; Frenking, G.; Harder, S. Dinitrogen complexation and reduction at low-valent calcium. *Science* **2021**, *371*, 1125−1128.

(4) Zhu, X.; Zhang, W.; Chen, H.; Mo, J. Impacts of nitrogen deposition on soil nitrogen cycle in forest ecosystems: A review. *Acta Ecol. Sin.* **2015**, *35*, 35−43.

(5) Nørskov, J. C. J.; Miranda, R.; Fitzsimmons, T.; Stack, R.*Sustainable Ammonia Synthesis − Exploring the scientific challenges associated with discovering alternative, sustainable processes for ammonia production*; U.S. Department of Energy: Dulles, Virginia, 2016.

(6) Ritchie, H. R. M.*CO and Greenhouse Gas Emissions*. Our World in Data, 2020. https://ourworldindata.org/co2-and-other-greenhouse-gas-emissions. (accessed 2022, 31st of March).

(7) Greenlee, L. F.; Renner, J. N.; Foster, S. L. The Use of Controls for Consistent and Accurate Measurements of Electrocatalytic Ammonia Synthesis from Dinitrogen. *ACS Catal.* **2018**, *8*, 7820−7827.

(8) MacFarlane, D. R.; Cherepanov, P. V.; Choi, J.; Suryanto, B. H. R.; Hodgetts, R. Y.; Bakker, J. M.; Ferrero Vallana, F. M.; Simonov, A. N. A Roadmap to the Ammonia Economy. *Joule* **2020**, 1−1205.

(9) Kyriakou, V.; Garagounis, I.; Vasileiou, E.; Vourros, A.; Stoukides, M. Progress in the Electrochemical Synthesis of Ammonia. *Catal. Today* **2017**, *286*, 2−13.

(10) Wang, M.; Khan, M. A.; Mohsin, I.; Wicks, J.; Ip, A. H.; Sumon, K. Z.; Dinh, C.-T.; Sargent, E. H.; Gates, I. D.; Kibria, M. G. Can sustainable ammonia synthesis pathways compete with fossil-fuel based Haber−Bosch processes? *Energy Environ. Sci.* **2021**, *14*, 2535−2548.

(11) Fernandez, C. A.; Hortance, N. M.; Liu, Y.-H.; Lim, J.; Hatzell, K. B.; Hatzell, M. C. Opportunities for intermediate temperature renewable ammonia electrosynthesis. *J. Mater. Chem. A* **2020**, *8*, 15591−15606.

(12) Zhou, F.; Azofra, L. M.; Ali, M.; Kar, M.; Simonov, A. N.; McDonnell-Worth, C.; Sun, C.; Zhang, X.; Macfarlane, D. R. Electro-synthesis of ammonia from nitrogen at ambient temperature and pressure in ionic liquids. *Energy Environ. Sci.* **2017**, *10*, 2516−2520.

(13) Suryanto, B. H. R.; Kang, C. S. M.; Wang, D.; Xiao, C.; Zhou, F.; Azofra, L. M.; Cavallo, L.; Zhang, X.; Macfarlane, D. R. Rational Electrode-Electrolyte Design for Efficient Ammonia Electrosynthesis under Ambient Conditions. *ACS Energy Lett.* **2018**, *3*, 1219−1224.

(14) König, M.; Vaes, J.; Klemm, E.; Pant, D. Solvents and Supporting Electrolytes in the Electrocatalytic Reduction of CO_2. *iScience* **2019**, *19*, 135−160.

(15) Andersen, S. Z.; Čolić, V.; Yang, S.; Schwalbe, J. A.; Nielander, A. C.; McEnaney, J. M.; Enemark-Rasmussen, K.; Baker, J. G.; Singh, A. R.; Rohr, B. A.; et al. A rigorous electrochemical ammonia synthesis protocol with quantitative isotope measurements. *Nature* **2019**, *570*, 504−508.

(16) Suryanto, B. H. R.; Wang, D.; Azofra, L. M.; Harb, M.; Cavallo, L.; Jalili, R.; Mitchell, D. R. G.; Chatti, M.; MacFarlane, D. R. MoS_2 Polymorphic Engineering Enhances Selectivity in the Electrochemical Reduction of Nitrogen to Ammonia. *ACS Energy Lett.* **2019**, *4*, 430−435.

(17) Einsle, O.; Tezcan, F. A.; Andrade, S. L. A.; Schmid, B.; Yoshida, M.; Howard, J. B.; Rees, D. C. Nitrogenase MoFe-Protein at 1.16 Å Resolution: A Central Ligand in the FeMo-Cofactor. *Science* **2002**, *297*, 1696−1700.

(18) Michalsky, R.; Zhang, Y. J.; Medford, A. J.; Peterson, A. A. Departures from the adsorption energy scaling relations for metal carbide catalysts. *J. Phys. Chem. C* **2014**, *118*, 13026−13034.

(19) Matanovic, I.; Garzon, F. H. Nitrogen electroreduction and hydrogen evolution on cubic molybdenum carbide: A density functional study. *Phys. Chem. Chem. Phys.* **2018**, *20*, 14679−14687.

(20) Li, Q.; Qiu, S.; He, L.; Zhang, X.; Sun, C. Impact of H-termination on the nitrogen reduction reaction of molybdenum carbide as an electrochemical catalyst. *Phys. Chem. Chem. Phys.* **2018**, *20*, 23338−23343.

(21) Du, H.-L.; Hodgetts, R. Y.; Chatti, M.; Nguyen, C. K.; Macfarlane, D. R.; Simonov, A. N. Is Molybdenum Disulfide Modified with Molybdenum Metal Catalytically Active for the Nitrogen Reduction Reaction? *J. Electrochem. Soc.* **2020**, *167*, 146507−146507.

(22) Du, H.; Yang, C.; Pu, W.; Zeng, L.; Gong, J. Enhanced Electrochemical Reduction of N 2 to Ammonia over Pyrite FeS_2 with Excellent Selectivity. *ACS Sustainable Chem. Eng.* **2020**, *8*, 10572−10580.

(23) Cheng, H.; Ding, L. X.; Chen, G. F.; Zhang, L.; Xue, J.; Wang, H. Molybdenum Carbide Nanodots Enable Efficient Electrocatalytic Nitrogen Fixation under Ambient Conditions. *Adv. Mater.* **2018**, *30*, 1−7.

(24) Peng, M.; Qiao, Y.; Luo, M.; Wang, M.; Chu, S.; Zhao, Y.; Liu, P.; Liu, J.; Tan, Y. Bioinspired Fe_3C@C as Highly Efficient Electrocatalyst for Nitrogen Reduction Reaction under Ambient Conditions. *ACS Appl. Mater. Int.* **2019**, *11*, 40062−40068.

(25) Choi, J.; Suryanto, B. H. R.; Wang, D.; Du, H. L.; Hodgetts, R. Y.; Ferrero Vallana, F. M.; MacFarlane, D. R.; Simonov, A. N. Identification and elimination of false positives in electrochemical nitrogen reduction studies. *Nat. Commun.* **2020**, *11*, 1−10.

(26) Chen, Y.; Liu, H.; Ha, N.; Licht, S.; Gu, S.; Li, W. Revealing nitrogen-containing species in commercial catalysts used for ammonia electrosynthesis. *Nat. Catal.* **2020**, 1−1061.

(27) Choi, J.; Choi, J.; Du, H. L.; Du, H. L.; Nguyen, C. K.; Nguyen, C. K.; Suryanto, B. H. R.; Simonov, A. N.; Simonov, A. N.; MacFarlane, D. R.; et al. Electroreduction of Nitrates, Nitrites, and Gaseous Nitrogen Oxides: A Potential Source of Ammonia in Dinitrogen Reduction Studies. *ACS Energy Lett.* **2020**, *5*, 2095−2097.

(28) Du, H. L.; Gengenbach, T. R.; Hodgetts, R.; Macfarlane, D. R.; Simonov, A. N. Critical Assessment of the Electrocatalytic Activity of Vanadium and Niobium Nitrides toward Dinitrogen Reduction to Ammonia. *ACS Sustainable Chem. Eng.* **2019**, *7*, 6839−6850.

(29) Yu, W.; Buabthong, P.; Read, C. G.; Dalleska, N. F.; Lewis, N. S.; Lewerenz, H.-J.; Gray, H. B.; Brinkert, K. Cathodic NH_4^+ leaching of nitrogen impurities in CoMo thin-film electrodes in aqueous acidic solutions. *Sustainable Energy Fuels* **2020**, *4*, 5080−5087.

(30) Hu, B.; Hu, M.; Seefeldt, L.; Liu, T. L. Electrochemical dinitrogen reduction to ammonia by Mo_2N: catalysis or decomposition? *ACS Energy Lett.* **2019**, *4*, 1053−1054.

(31) Qin, B.; Li, Y.; Zhang, Q.; Yang, G.; Liang, H.; Peng, F. Understanding of nitrogen fixation electro catalyzed by molybdenum−iron carbide through the experiment and theory. *Nano Energy* **2020**, *68*, No. 104374.

(32) Zhang, Y.; Hu, J.; Zhang, C.; Cheung, A. T. F.; Zhang, Y.; Liu, L.; Leung, M. K. H. Mo_2C embedded on nitrogen-doped carbon toward electrocatalytic nitrogen reduction to ammonia under ambient conditions. *Int. J. Hydrogen Energy* **2021**, *46*, 13011−13019.

(33) Ba, K.; Wang, G.; Ye, T.; Wang, X.; Sun, Y.; Liu, H.; Hu, A.; Li, Z.; Sun, Z.Single Faceted Two-Dimensional Mo_2C Electrocatalyst for Highly Efficient Nitrogen Fixation. 2020, *10* (14), 7864−7870, DOI: 10.1021/acscatal.0c01127.

(34) Liu, Y.; Zhu, X.; Zhang, Q.; Tang, T.; Zhang, Y.; Gu, L.; Li, Y.; Bao, J.; Dai, Z.; Hu, J. S. Engineering Mo/Mo_2C/MoC hetero-interfaces for enhanced electrocatalytic nitrogen reduction. *J. Mater. Chem. A* **2020**, *8*, 8920−8926.

(35) Wang, T.; Kou, Z.; Zhang, J.; Wang, H.; Zeng, Y. J.; Wei, S.; Zhang, H. Boosting Faradic efficiency of dinitrogen reduction on the negatively charged Mo sites modulated via interstitial Fe doping into a Mo_2C nanowall catalyst. *Chem. Eng. J.* **2021**, *417*, 127924−127924.

(36) Qu, X.; Shen, L.; Mao, Y.; Lin, J.; Li, Y.; Li, G.; Zhang, Y.; Jiang, Y.; Sun, S. Facile Preparation of Carbon Shells-Coated O-Doped Molybdenum Carbide Nanoparticles as High Selective Electro-

https://doi.org/10.1021/acscatal.2c04491
ACS Catal. 2023, 13, 1649−1661

catalysts for Nitrogen Reduction Reaction under Ambient Conditions. *ACS Appl. Mater. Interfaces* **2019**, *11*, 31869−31877.
(37) Cong, L.; Yu, Z.; Liu, F.; Huang, W. Electrochemical synthesis of ammonia from N_2 and H_2O using a typical non-noble metal carbon-based catalyst under ambient conditions. *Catal. Sci. Technol.* **2019**, *9*, 1208−1208.
(38) Biswas, A.; Bhardwaj, S.; Boruah, T.; Dey, R. S. Electrochemical ammonia synthesis: Fundamental practices and recent developments in transition metal boride, carbide and nitride-class of catalysts. *Mater. Adv.* **2022**, *3*, 5207.
(39) Gómez-Marín, A. M.; Ticianelli, E. A. Analysis of the electrocatalytic activity of α-molybdenum carbide thin porous electrodes toward the hydrogen evolution reaction. *Electrochim. Acta* **2016**, *220*, 363−372.
(40) Kraupner, A.; Markus, A.; Palkovits, R.; Schlicht, K.; Giordano, C. Mesoporous Fe3C sponges as magnetic supports and as heterogeneous catalyst. *J. Mater. Chem.* **2010**, *20*, 6019−6022.
(41) Snovski, R.; Grinblat, J.; Sougrati, M. T.; Jumas, J. C.; Margel, S. Synthesis and characterization of iron, iron oxide and iron carbide nanostructures. *J. Magn. Magn. Mater.* **2014**, *349*, 35−44.
(42) Klencsar, Z. Mössbauer spectrum analysis by evolution algorithm. *Nucl. Instrum. Methods Phys. Res., Sect. B* **1997**, *129*, 527−533.
(43) Kuhl, K. P.; Cave, E. R.; Abram, D. N.; Jaramillo, T. F. New insights into the electrochemical reduction of carbon dioxide on metallic copper surfaces. *Energy Environ. Sci.* **2012**, *5*, 7050−7059.
(44) Cai, X.; Iriawan, H.; Yang, F.; Luo, L.; Shen, S.; Shao-Horn, Y.; Zhang, J. Interaction of Ammonia with Nafion and Electrolyte in Electrocatalytic Nitrogen Reduction Study. *J. Phys. Chem. Lett.* **2021**, *12*, 6861−6866.
(45) Liu, H.; Zhang, Y.; Luo, J. The removal of inevitable NO_x species in catalysts and the selection of appropriate membrane for measuring electrocatalytic ammonia synthesis accurately. *J. Energy Chem.* **2020**, *49*, 51−58.
(46) Izelaar, B.; Ripepi, D.; van Noordenne, D. D.; Jungbacker, P.; Kortlever, R.; Mulder, F. M.Determining sources of NO_x and NH_3 impurities and removal strategies for reliable electrochemical NRR. *In Submission*2022.
(47) Li, L.; Tang, C.; Yao, D.; Zheng, Y.; Qiao, S. Z. Electrochemical Nitrogen Reduction: Identification and Elimination of Contamination in Electrolyte. *ACS Energy Lett.* **2019**, *4*, 2111−2116.
(48) Weatherburn, M. W. Phenol-Hypochlorite Reaction for Determination of Ammonia. *Anal. Chem.* **1967**, *39*, 971−974.
(49) Kyotani, T.; Nagai, T.; Inoue, S.; Tomita, A. Formation of new type of porous carbon by carbonization in zeolite nanochannels. *Chem. Mater.* **1997**, *9*, 609−615.
(50) Kim, J. H.; Ju, H.; An, B.-S.; An, Y.; Cho, K.; Kim, S. H.; Bae, Y.-S.; Yoon, H. C. Comparison between Fe_2O_3/C and Fe_3C/Fe_2O_3/Fe/C Electrocatalysts for N_2 Reduction in an Alkaline Electrolyte. *ACS Appl. Mater. Interfaces* **2021**, 61316−61316.
(51) Kniep, B.; Constantinescu, A.; Niemeier, D.; Becker, K. D. An in-situ Mössbauer study of the formation of cementite, Fe_3C. *Z. Anorg. Allg. Chem.* **2003**, *629*, 1795−1804.
(52) Muxworthy, A. R.; Schmidbauer, E.; Petersen, N. Magnetic properties and Mössbauer spectra of urban atmospheric particulate matter: A case study from Munich, Germany. *Geophys. J. Int.* **2002**, *150*, 558−570.
(53) Kuivila, C. S.; Butt, J. B.; Stair, P. C. Characterization of surface species on iron synthesis catalysts by X-ray photoelectron spectroscopy. *Appl. Surf. Sci.* **1988**, *32*, 99−121.
(54) Malina, O.; Jakubec, P.; Kašlík, J.; Tuček, J.; Zbořil, R. A simple high-yield synthesis of high-purity Hägg carbide (χ-Fe_5C_2) nanoparticles with extraordinary electrochemical properties. *Nanoscale* **2017**, *9*, 10440−10446.
(55) Goya, G. F.; Berquó, T. S.; Fonseca, F. C.; Morales, M. P. Static and dynamic magnetic properties of spherical magnetite nanoparticles. *J. Appl. Phys.* **2003**, *94*, 3520−3528.
(56) Choi, J. G.; Choi, D.; Thompson, L. T. Surface properties of high-surface-area powder and thin film molybdenum nitrides treated in H_2 and H_2S. *Appl. Surf. Sci.* **1997**, *108*, 103−111.
(57) Wan, C.; Regmi, Y. N.; Leonard, B. M. Multiple phases of molybdenum carbide as electrocatalysts for the hydrogen evolution reaction. *Am. Ethnol.* **2014**, *126*, 6525−6528.
(58) Seh, Z. W.; Fredrickson, K. D.; Anasori, B.; Kibsgaard, J.; Strickler, A. L.; Lukatskaya, M. R.; Gogotsi, Y.; Jaramillo, T. F.; Vojvodic, A. Two-Dimensional Molybdenum Carbide (MXene) as an Efficient Electrocatalyst for Hydrogen Evolution. *ACS Energy Lett.* **2016**, *1*, 589−594.
(59) Saji, V. S.; Lee, C. W. Molybdenum, molybdenum oxides, and their electrochemistry. *ChemSusChem* **2012**, *5*, 1146−1161.
(60) Nishimoto, M.; Muto, I.; Sugawara, Y.; Hara, N. Morphological Characteristics of Trenching around MnS Inclusions in Type 316 Stainless Steel: The Role of Molybdenum in Pitting Corrosion Resistance. *J. Electrochem. Soc.* **2019**, *166*, C3081−C3089.
(61) Biesinger, M. C.; Payne, B. P.; Grosvenor, A. P.; Lau, L. W. M.; Gerson, A. R.; Smart, R. S. C. Resolving surface chemical states in XPS analysis of first row transition metals, oxides and hydroxides: Cr, Mn, Fe, Co and Ni. *Appl. Surf. Sci.* **2011**, *257*, 2717−2730.
(62) Townsend, H. E. Potential-pH diagrams at elevatedtemperature for the system Fe-H_2O. *Corros. Sci.* **1970**, *10*, 343−358.
(63) Xu, W.; Street, S. R.; Amri, M.; Mosselmans, J. F. W.; Quinn, P. D.; Rayment, T.; Davenport, A. J. In-Situ Synchrotron Studies of the Effect of Nitrate on Iron Artificial Pits in Chloride Solutions. *J. Electrochem. Soc.* **2015**, *162*, C243−C250.
(64) Vrubel, H.; Hu, X. Molybdenum boride and carbide catalyze hydrogen evolution in both acidic and basic solutions. *Angew. Chem. Int. Ed.* **2012**, *51*, 12703−12706.
(65) Bard, A. J.; Inzelt, G.; Scholz, F.*Electrochemical dictionary*; Springer, 2012, DOI: 10.1007/978-3-642-29551-5.
(66) Skúlason, E.; Bligaard, T.; Gudmundsdóttir, S.; Studt, F.; Rossmeisl, J.; Abild-Pedersen, F.; Vegge, T.; Jónsson, H.; Nørskov, J. K. A theoretical evaluation of possible transition metal electrocatalysts for N2 reduction. *Phys. Chem. Chem. Phys.* **2012**, *14*, 1235−1245.
(67) Ko, B. H.; Hasa, B.; Shin, H.; Zhao, Y.; Jiao, F. Electrochemical Reduction of Gaseous Nitrogen Oxides on Transition Metals at Ambient Conditions. *J. Am. Chem. Soc.* **2022**, *144*, 1258−1266.
(68) Dima, G. E.; De Vooys, A. C. A.; Koper, M. T. M. Electrocatalytic reduction of nitrate at low concentration on coinage and transition-metal electrodes in acid solutions. *J. Electroanal. Chem.* **2003**, *554-555*, 15−23.
(69) Zheng, W.; Cotter, T. P.; Kaghazchi, P.; Jacob, T.; Frank, B.; Schlichte, K.; Zhang, W.; Su, D. S.; Schüth, F.; Schlögl, R. Experimental and theoretical investigation of molybdenum carbide and nitride as catalysts for ammonia decomposition. *J. Am. Chem. Soc.* **2013**, *135*, 3458−3464.
(70) Wang, Y.; Zhang, L.; Niu, Y.; Fang, D.; Wang, J.; Su, Q.; Wang, C. Boosting NH3 production from nitrate electroreduction via electronic structure engineering of Fe_3C nanoflakes. *Green Chem.* **2021**, *23*, 7594−7608.
(71) Hodgetts, R. Y.; Du, H. L.; MacFarlane, D. R.; Simonov, A. N. Electrochemically Induced Generation of Extraneous Nitrite and Ammonia in Organic Electrolyte Solutions During Nitrogen Reduction Experiments. *ChemElectroChem* **2021**, *2*, 1−10.
(72) Dabundo, R.; Lehmann, M. F.; Treibergs, L.; Tobias, C. R.; Altabet, M. A.; Moisander, P. H.; Granger, J. The Contamination of Commercial $^{15}N_2$ Gas Stocks with ^{15}N−Labeled Nitrate and Ammonium and Consequences for Nitrogen Fixation Measurements. *PLoS One* **2014**, *9*, e110335−e110335.
(73) Hanifpour, F.; Sveinbjörnsson, A.; Canales, C. P.; Skúlason, E.; Flosadóttir, H. D. Preparation of Nafion Membranes for Reproducible Ammonia Quantification in Nitrogen Reduction Reaction Experiments. *Angew. Chem., Int. Ed.* **2020**, *59*, 22938−22942.
(74) Licht, S.; Cui, B.; Wang, B.; Li, F.-F.; Lau, J.; Liu, S. Ammonia synthesis by N_2 and steam electrolysis in molten hydroxide suspensions of nanoscale Fe_2O_3. *Science* **2014**, *345*, 637−640.

https://doi.org/10.1021/acscatal.2c04491
ACS Catal. 2023, 13, 1649−1661

(75) Hueso, J. L.; Espinós, J. P.; Caballero, A.; Cotrino, J.; González-Elipe, A. R. XPS investigation of the reaction of carbon with NO, O_2, N_2 and H_2O plasmas. *Carbon* **2007**, *45*, 89−96.
(76) Chastain, J.; King, Jr, R. C.*Handbook of X-ray photoelectron spectroscopy*; Perkin-Elmer Corporation1992, *40*, 221.
(77) Bertóti, I. Characterization of nitride coatings by XPS. *Surf. Coat. Technol.* **2002**, *151-152*, 194−203.
(78) Burshtein, T. Y.; Aias, D.; Wang, J.; Sananis, M.; Farber, E. M.; Gazit, O. M.; Grinberg, I.; Eisenberg, D. Fe−N−C electrocatalysts in the oxygen and nitrogen cycles in alkaline media: the role of iron carbide. *Phys. Chem. Chem. Phys.* **2021**, *23*, 26674−26679.
(79) Wu, Z. Y.; Xu, X. X.; Hu, B. C.; Liang, H. W.; Lin, Y.; Chen, L. F.; Yu, S. H. Iron carbide nanoparticles encapsulated in mesoporous Fe-N-doped carbon nanofibers for efficient electrocatalysis. *Am. Ethnol.* **2015**, *127*, 8297−8301.
(80) Jiang, W.-J.; Gu, L.; Li, L.; Zhang, Y.; Zhang, X.; Zhang, L.-J.; Wang, J.-Q.; Hu, J.-S.; Wei, Z.; Wan, L.-J. Understanding the high activity of Fe−N−C electrocatalysts in oxygen reduction: Fe/Fe_3C nanoparticles boost the activity of $Fe−N_x$. *J. Am. Chem. Soc.* **2016**, *138*, 3570−3578.

https://doi.org/10.1021/acscatal.2c04491
ACS Catal. 2023, 13, 1649−1661